The Astrophysical Journal, 924:106 (11pp), 2022 January 10 https://doi.org/10.3847/1538-4357/ac374d

© 2022. The Author(s). Published by the American Astronomical Society.

OPEN ACCESS

The Solar Eruption of 2017 September 10: Wavy with a Chance of Protons

Curt A. de Koning[1,2], V. J. Pizzo[2], and Daniel B. Seaton[1,3]

[1] Cooperative Institute for Research in Environmental Sciences, University of Colorado Boulder, CO, 80309, USA; curt.a.dekoning@noaa.gov
[2] NOAA/Space Weather Prediction Center Boulder, CO, 80305, USA
[3] NOAA/National Centers for Environmental Information Boulder, CO, 80305, USA

Received 2020 July 14; revised 2021 October 22; accepted 2021 November 5; published 2022 January 17

Abstract

High-resolution SUVI images reveal an interesting new picture of particle acceleration in powerful solar eruptions. Typically, powerful solar eruptions include a coronal wave component, as well the traditional CME and flare components. At low solar altitudes, coronal waves refract downward, toward the solar surface, because of the slower Alfvén speeds at the base of the corona. The refracted wave plus the shock wave ahead of an intense CME allow for a two-step shock acceleration process that can result in relativistic or GLE particles. This mechanism may be particularly applicable to the first-to-arrive, prompt relativistic particles measured by the Fort Smith neutron monitor during GLE # 72 on 2017 September 10.

Unified Astronomy Thesaurus concepts: Solar storm (1526); Solar coronal waves (1995); Solar particle emission (1517)

1. Introduction

From 2017 September 4–9, as NOAA Active Region (AR) 12673 moved across the visible solar disk, it produced a series of explosive events, including 29 C-class flares, 14 M-class flares, an X9.3, an X2.2, and an X1.3 flare, as well four coronal mass ejections (CMEs). Finally, on September 10, after moving 1° behind the western limb of the Sun, AR 12673 went out with a bang, producing a final series of explosive events consisting of five C-class flares, an X8.2 flare, a CME, and a large-scale coronal wave (LSCW) that reached super-Alfvénic speeds. This solar eruption—that is, the large-scale, rapid or impulsive rearrangement of the solar magnetic field—also spawned strong solar particle emissions, including solar energetic particles (SEPs) and a ground-level event (GLE).

The solar eruption of 2017 September 10 has been studied extremely well: from radio/microwave, to white light, to ultraviolet/extreme ultraviolet (UV/EUV), to X-rays, to γ-rays; from the Sun, through space, to Earth, and beyond; from the flare, to the coronal wave, to the CME, to the SEP/GLE; for basic research and for space weather forecasting. (See Berger et al. 2018; Chamberlin et al. 2018; Chertok 2018; Cohen & Mewaldt 2018; Gary et al. 2018; Gopalswamy et al. 2018; Goryaev et al. 2018; Guo et al. 2018; Jiggens et al. 2018; Kurt et al. 2018; Lee et al. 2018; Liu et al. 2018; Li et al. 2018; Long et al. 2018; Longcope et al. 2018; Mavromichalaki et al. 2018; Mishev et al. 2018; Mishev & Usoskin 2018; Omodei et al. 2018; Polito et al. 2018; Seaton & Darnel 2018; Veronig et al. 2018; Warren et al. 2018; Yan et al. 2018; Zhao et al. 2018; Bruno et al. 2019; Hu et al. 2019; Kurt et al. 2019; Li et al. 2019; Morosan et al. 2019; Starodubtsev et al. 2019; Wu et al. 2019; Kocharov et al. 2020; Kouloumvakos et al. 2020; Perez-Peraza et al. 2020). In spite of the thorough and in-depth examination of this event, one aspect that has not been commented on is the possibility that the LSCW influenced the GLE. Using high-resolution pictures from the new Solar Ultraviolet Imager (SUVI) on board the Geostationary Operational Environmental Satellite (GOES)-16 spacecraft, we present evidence that suggests the relativistic particles observed by neutron monitors were accelerated by the shocked LSCW. In Section 2, we show that the LSCW is an encompassing, dome-shaped wave. In Section 4, we adopt the idea of Vainio & Khan (2004), and suggest that GLE particles were accelerated in a two-step process: first, downstream of the refracted base of the LSCW, and subsequently, higher in the corona by the dome of the LSCW. In the ensuing Discussion and Conclusion sections, we encourage researchers and modellers to look beyond flares and CME-driven shocks as the only mechanisms to accelerate solar cosmic rays and consider also LSCWs as a possible mechanism.

Before we proceed to Section 2 and a description of the data used in this research, we will briefly cover some background material related to the acceleration and measurement of solar cosmic rays. Neutron monitors are ground-based instruments used to record cosmic ray intensity. In particular, neutron monitors measure the low-energy nucleonic component of the secondary particle cascade initiated when a primary cosmic ray is incident on the top of the Earth's atmosphere (Simpson et al. 1953). The minimum energy, or cutoff energy, of the primary cosmic ray that neutron monitors respond to depends on the geomagnetic latitude and atmospheric depth at its placement. The neutron monitor cutoff is usually reported in units of magnetic rigidity, $R = p/q$, where p and q are the particle momentum and charge, respectively. Qualitatively, a particle with higher rigidity will have a higher resistance to deflection by a magnetic field. For sea-level high-latitude neutron monitors, the atmospheric cutoff dominates the geomagnetic cutoff; these stations respond to primary cosmic rays with rigidity greater than 1 GV, or equivalently, kinetic energy greater than 433 MeV. Equatorial neutron monitors can have cutoff rigidities as high as 17 GV, such as the Princess Sirindhorn neutron monitor atop Doi Inthanon, Thailand's highest mountain.

Because of these high cutoff rigidities, neutron monitors generally measure galactic cosmic ray intensities. However, occasionally, particles emitted from the Sun will be accelerated

Original content from this work may be used under the terms of the Creative Commons Attribution 4.0 licence. Any further distribution of this work must maintain attribution to the author(s) and the title of the work, journal citation and DOI.

to relativistic energies and affect the neutron monitor count rate. Such events are known as ground-level events, or GLEs. At the time of this publication, there have been 72 recorded GLEs, with the event of 2017 September 10 being the 72nd. The first GLE observed by the neutron monitor network occurred on 1956 February 23. It was the fifth recorded GLE; the first four occurred prior to the neutron monitor era and were observed by ionization chambers or muon telescopes.

Historically, the acceleration of solar protons to relativistic energies, or GLE particles, has been attributed to either direct acceleration during the flare energy release or to acceleration by a CME-driven shock wave in the high corona (see, for example, Miroshnichenko 2018, written for the 75th anniversary of the first GLE). This debate continues even today, as illustrated by the various conclusions reached concerning particle acceleration during the solar eruption of 2017 September 10. Most researchers conclude the CME-driven shock contributed to the acceleration of solar particles to relativistic energies; however, a few researchers conclude that the particle observations are consistent with acceleration by the flare.

Perez-Peraza et al. (2020) adjusted theoretical spectra to match the observed energy spectrum derived from GOES and neutron monitor data. They conclude there were two different particle populations present during the GLE of 2017 September 10, each with a different energy spectrum. These spectra could have come from several possible acceleration scenarios, some of which involve shock acceleration. But Perez-Peraza et al. (2020) point out that a single acceleration mechanism, via reconnection in the current sheet typical of the flare plasma region, cannot be disregarded. This single mechanism would operate in two acceleration stages, to account for the two particle populations.

Zhao et al. (2018) used solar proton data from GOES and the neutron monitor network, along with near-relativistic electron data from ACE to estimate particle onset times at different energies. By comparing the particle onset times to soft and hard X-ray data and radio burst data, they conclude that the first arriving relativistic and nonrelativistic protons and electrons may have been accelerated by the solar flare. In fact, based on the flare location near the western limb of the Sun, they state that if particles were accelerated by a shock, they would have to be accelerated by a shock driven by the east flank of the CME, which would be a weak shock that could hardly accelerate protons to relativistic energies. Zhao et al. (2018) also conclude that "interaction of the CME with structures higher in the corona could not have played a role in accelerating the first arriving high-energy protons."

Even when it is concluded that the particles were accelerated by the CME-driven shock, different researchers suggest different locations along the shock front where particle acceleration occurred, and many researchers suggest additional acceleration processes prior to shock acceleration.

Kouloumvakos et al. (2020) suggest that the CME-driven shock was the singular source for all relativistic protons, including those that produced γ-rays at the Sun and GLE particles at Earth. The large-scale characteristics of the CME-driven shock were derived from EUV and white-light observations made by SDO, SOHO, and STEREO-A. They then undertook extensive modeling of the shock parameters to show variations along the shock front of the Alfvénic Mach number, the density compression ratio, and the angle of the magnetic field relative to the shock normal. They also estimated the shock front's magnetic connection to the visible solar surface—for γ-ray production—and to the Earth—for GLE arrival. Kouloumvakos et al. (2020) estimated that the shock first intersected field lines that were connected to Earth at 15:57 UT (note that this time, and all times mentioned in our paper, are for an observer at L1 or Earth), suggesting that GLE particle release occurred quite early. According to their analysis, the first relativistic protons reached Earth at 16:08:30 UT, the time that Kouloumvakos et al. (2020) suggest the Fort Smith neutron monitor count rate started to increase. As they point out, 450 MeV protons traveling along the nominal Archimedean spiral should only add ~4 minutes onto the light travel time; that is, relativistic protons could be observed at Earth as early as 16:01 UT. To account for the delay between earliest possible arrival of relativistic particles at Earth and observed arrival time, Kouloumvakos et al. (2020) require a longer path length than provided by a simple Parker spiral. They suggest that a longer path length can be achieved by assuming that the protons spiraled around a toroidal flux rope from one of several CMEs in the days preceding the 2017 September 10 solar eruption and by assuming pitch-angle scattering in the turbulent interplanetary medium. Finally, to approximate not only the arrival time of the shock-accelerated protons with the Fort Smith neutron monitor observations, but also the shape of the observed time-intensity profile, Kouloumvakos et al. (2020) estimate that direct-flare acceleration of protons contributed about $29 \pm 8\%$ of the observed neutron monitor counts.

Gopalswamy et al. (2018) suggest a single particle acceleration mechanism that occurred at the eastern flank of the shock, when it crossed the Sun–Earth field line—the idea that was explicitly rejected by Zhao et al. (2018). Gopalswamy et al. (2018) suggest that solar particle release was at 16:05 UT, at a height of $4.4 \pm 0.4\,R_\odot$. They also suggest that poor longitudinal and latitudinal connectivity resulted in a low-intensity GLE with a softer-than-average fluence spectrum.

Augusto et al. (2019) suggest particle acceleration on the western edge of the solar disk, presumably near the nose of the CME shock. Although this region was not magnetically connected to the Earth, it was within the heliospheric current sheet (HCS). Furthermore, the flare and CME happened when Earth was crossing the HCS. In other words, Augusto et al. (2019) suggest that even though the active region had a poor magnetic connection with Earth, since the event was within an HCS structure, relativistic solar particles reached Earth and triggered a GLE because the HCS played the role of the Sun–Earth magnetic connection.

Kurt et al. (2019) analyzed neutron monitor data (Kurt et al. 2018), GOES-13 satellite data, and neutral emission data—X-ray and γ-ray (Omodei et al. 2018). They suggest that solar protons directly accelerated by the flare formed a seed population that was further accelerated by the CME-driven shock. Some of these reaccelerated protons returned to the Sun to produce the late phase of 100 MeV γ-ray emission, while other reaccelerated protons ended up on open field lines, with a path length of 1.5 ± 0.3 au, that produced the first GLE particles arriving at Earth.

Based on neutron monitor (Mishev et al. 2018) and γ-ray (Omodei et al. 2018) data, Kocharov et al. (2020) suggested that the GLE of 2017 September 10 had a prompt and a delayed component. The first, prompt solar protons were injected directly onto the Sun–Earth magnetic field line and streamed along that field line with a relatively narrow pitch-angle distribution. The primary focus of Kocharov et al. (2020) is the delayed component, which they suggest began after 17:10 UT. Based on extensive modeling of the neutron monitor response (Mishev et al. 2018), Kocharov et al. (2020) infer that the delayed component had a broad pitch-angle distribution. Furthermore, they infer that the maximum phase of the delayed component coincided with the maximum phase of the observed long-duration >100 MeV γ-ray emission. In their opinion, this suggests that the >300 MeV protons at the Sun—which trigger nuclear interactions at the Sun, resulting in pion-decay γ-rays—and the >400 MeV protons at the Earth—which trigger a nuclear cascade at the Earth, resulting in GLEs—had a common source behind the CME. This is in contrast to Kurt et al. (2019), who placed the common source ahead of the CME. One possibility, which Kocharov et al. (2020) claim has not received sufficient attention, is that the delayed component was produced by reacceleration of energetic particles originating in the CME-trailing current sheet that formed above the flaring region. The subsequent cross-field propagation of the delayed component, from its source on the western solar limb to the Earth, was modeled as cross-field diffusion.

The range of acceleration scenarios we have just described is not meant to be an exhaustive discussion of all possible mechanisms; rather, these are the scenarios that have been suggested thus far (through the end of 2020) for this particular GLE. In this paper, we suggest another particle acceleration mechanism that was active during the solar eruption of 2017 September 10, which has not yet received sufficient attention, namely solar proton acceleration in the low corona by the LSCW. The suggestion that coronal waves can accelerate protons is itself not a new idea. Particle acceleration by coronal waves, sometimes called coronal Moreton waves, EIT waves, and EUV waves, was first suggested by Kocharov et al. (1994). Using the data available to them from the solar particle event of 1990 May 24, Kocharov et al. (1994) suggested that the most natural, and hence most probable, acceleration scenario for electrons, protons, and neutrons—including relativistic protons and direct solar neutrons observed by the Climax neutron monitor (GLE # 48)—was shock acceleration by the observed Moreton wave. This idea received additional consideration by Cliver et al. (1995), who analyzed certain large SEPs that rapidly propagated more than 100° in longitude from the Hα flare site to the Sun–Earth field line. They concluded that these events provide indirect evidence for SEP acceleration by quasi-circumsolar coronal shock waves and that Moreton waves provide visible evidence of the propagating acceleration front. Later, Torsti et al. (1999) analyzed the SEP event of 1997 September 24, which included observations of 10–100 MeV protons and a concurrent EIT wave. They concluded that this event resulted from two periods of proton acceleration: the first injection, which had a hard spectrum, corresponded to an impulse that the launching CME imparted to the lower corona; the second injection, which had a softer spectrum, was delayed relative to the CME launch and occurred as the CME-driven shock expanded far away from the Sun. Recently, Park et al. (2015) used STEREO and SDO observations to measure the propagation of EUV waves across the Sun during 16 large, gradual SEP events. They concluded that EUV waves affected SEP acceleration since the 6–10 MeV SEP peak flux increased with increasing EUV wave speed and the proton spectral indices measured at higher energies became harder with increasing EUV wave speed. Other researchers have also found results that support the idea that proton SEPs are accelerated by large coronal shock waves (Torsti et al. 1998; Cliver 2001; Rouillard et al. 2012; Park et al. 2013; Warmuth 2015).

However, based on 26 eastern SEP events that had no direct magnetic connection to Earth, Miteva et al. (2014) reached an, at best, mixed conclusion. Although the arrival time of the EIT wave at the footpoint of the Sun–Earth field line was generally consistent with onset of the proton events, this was not the case for the electron events. In addition, the near-relativistic electron events did not become adiabatically focused during interplanetary propagation, as is the case for most western SEP events, suggesting that these electrons were not accelerated by the coronal wave in the vicinity of the Sun–Earth magnetic footpoint. Thus, Miteva et al. (2014) conclude that their survey "contradicts the role of an EIT wave, whatever its nature, as the principal SEP accelerator in cases where the particles come from poorly connected eruptive activity."

As we consider the role of the LSCW in accelerating solar protons to relativistic energies, we will focus particularly on the first-to-arrive GLE particles that were observed by the Fort Smith neutron monitor. Fort Smith is a neutron monitor in the Northwest Territories, Canada, just north of the Territories border with Alberta. It is part of the Spaceship Earth network (Bieber & Evenson 1995). Since this is a high-latitude station, the minimum energy observed by this neutron monitor is determined by the atmospheric cutoff of 433 MeV. To analyze the intensity–time profile of a neutron monitor, it is important to consider its asymptotic directions of approach. The asymptotic directions of approach indicate the location in the outer magnetosphere where particles of a particular energy must have originated in order to be observed at the neutron monitor in question after gyrating through the magnetosphere. Several researchers have shown that the asymptotic directions of approach for the Fort Smith neutron monitor were well-aligned with the Sun–Earth magnetic field line (Mishev et al. 2018; Kurt et al. 2019). Although there were other neutron monitors in the Spaceship Earth network with relatively nearby asymptotic directions of approach—Inuvik, Nain, Peawanuck—these stations did not see the onset of the GLE until many minutes after it was observed by Fort Smith. As other researchers have mentioned, this indicates that the initial relativistic particles observed by Fort Smith were confined to a narrow, field-aligned beam (Kurt et al. 2018, 2019; Mishev et al. 2018; Kocharov et al. 2020). Such a beam suggests a short-lived acceleration mechanism that injects particles directly at the base of the Sun–Earth field line. As we will describe in the following sections, one way to achieve such a beam is through an LSCW that accelerates particles in two steps as it sweeps over the Sun–Earth footpoint.

2. Examination of GOES-16/SUVI Images

An LSCW originated from the vicinity of AR 12673 at 15:52 UT (Liu et al. 2018; Seaton & Darnel 2018; Veronig et al. 2018). The LSCW was detected at several wavelengths by GOES-16, including 195 Å and 284 Å, which are shown in Figure 1. The left-hand panel (a) shows a specially processed, intrinsic brightness image (Seaton & Darnel 2018). While retaining its natural appearance and avoiding running-difference artifacts, this image still reveals dynamic features such as

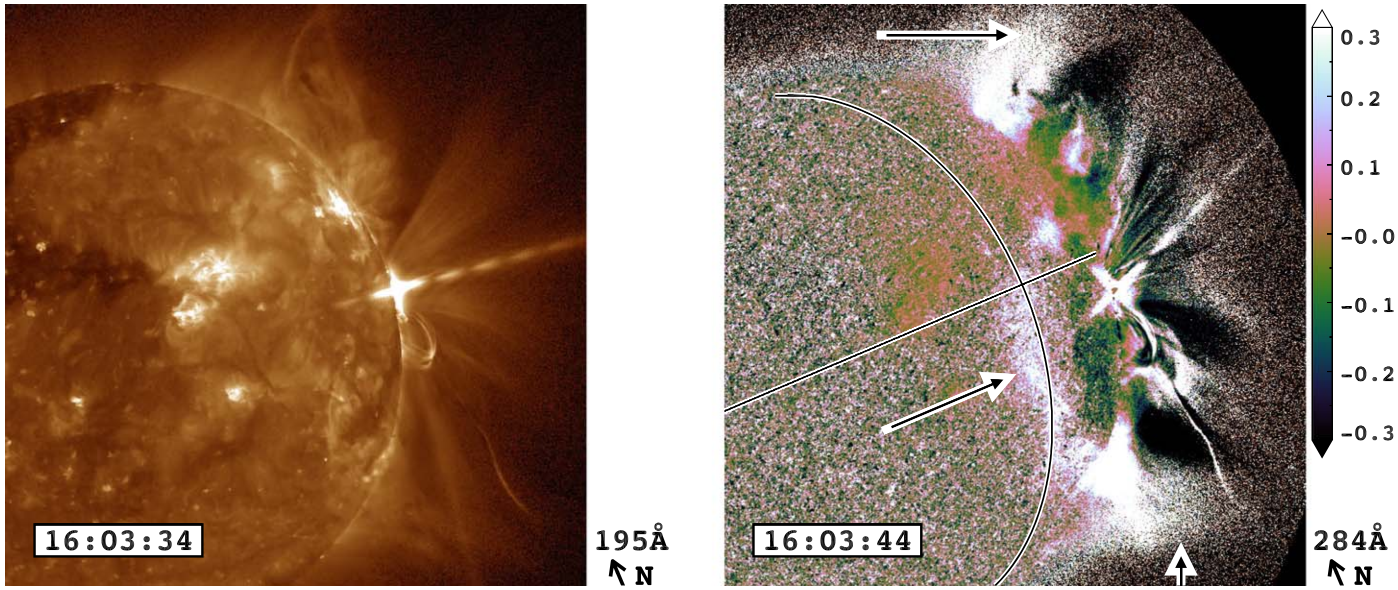

(a) (b)

Figure 1. (a) The large-scale coronal wave detected in the GOES-16 195 Å passband at 16:03:34 UT. In this specially processed (see Seaton & Darnel 2018, for processing details), intrinsic brightness image, which retains its natural appearance, dynamic features, such as the coronal wave, are visible over the solar limb. (b) The large-scale coronal wave detected in the GOES-16 284 Å passband at 16:03:44 UT. Whereas panel (a) showed an intrinsic brightness image, this running relative-difference image has enhanced the leading edge of the wave, especially on the solar disk; the leading edge of the wave shows up as the broad, curved, white feature indicated by the on-disk arrow. Arrows also indicate the northern and southern extent of the wave in the plane of the sky. According to the color scale to the right of the relative-difference image, the white regions have undergone a ⩾30% increase in intensity compared to the previous time step. The white/black lines show a circle of latitude—the solar equator—and a circle of longitude—40° west of the Sun–Earth line. The intersection of these two great circles indicates the nominal footpoint of the Parker spiral magnetic field. The orientation of solar north, in these and all subsequent SUVI images, is shown in the legend at the bottom right-hand corner of the images.

the LSCW. In contrast, the right-hand panel (b) is a relative running-difference image,

$$\Delta I = \frac{I(t_2) - I(t_1)}{I(t_1)}, \tag{1}$$

where $I(t_2)$ is the image of interest and $I(t_1)$ is the immediately preceding image. Although the relative running-difference image displays the black/white banding characteristic of running difference images, it also shows a much starker wave signature on the solar limb—and especially on the solar disk. As the LSCW spread outward across the solar disk, by 16:04 UT it reached the nominal footpoint of the Parker spiral magnetic field, assumed to be ~40° west of the Sun–Earth line, which can be estimated from the solar wind speed of 575 km s^{-1} observed at that time by the Advanced Composition Explorer (ACE) spacecraft (Stone et al. 1998). The assumed footpoint of the Parker field is shown in Figure 1(b) as the intersection of the solar equator and the circle of longitude. Shortly thereafter, at 16:10 UT, the neutron monitor whose asymptotic cone most nearly aligned with the Parker field—at that time, Fort Smith—observed the first solar cosmic rays (Kurt et al. 2018, 2019; Mishev et al. 2018; Kocharov et al. 2020; Zhao et al. 2018); the onset of GLE # 72 at Fort Smith is shown in Figure 2.

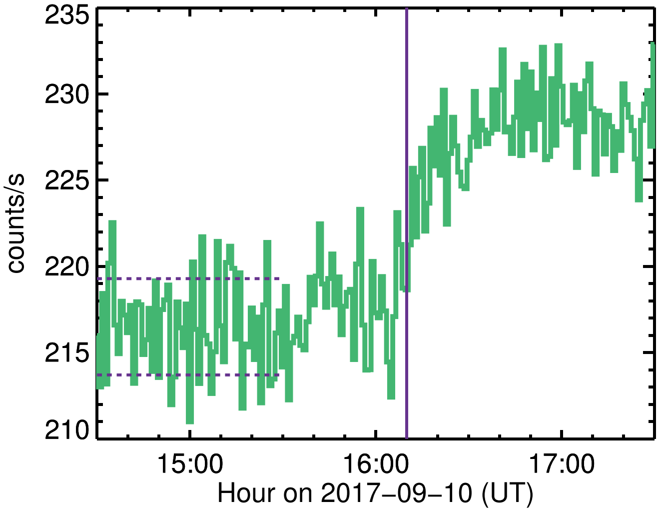

Figure 2. The corrected neutron monitor count rate measured at Fort Smith. This is the first neutron monitor to observe the onset of GLE # 72. The background count rate was taken to be the average count rate recorded from 14:30–15:30 UT; this time range was chosen to avoid the possibly nonrandom increase and subsequent decrease observed from about 15:30 UT until just after 16:00 UT. The horizontal dashed lines indicate the spread in the average count rate—the bottom line shows the average count rate minus one standard deviation, while the top line shows the average count rate plus one standard deviation. The solid vertical line at 16:10 UT indicates the time when the count rate started to rise significantly above the background level.

As explained in more detail in Section 4, we assume the particles were accelerated by the LSCW when the shock wave passed over the Sun–Earth footpoint. Accounting for light-travel time, the observations of the LSCW near the Sun–Earth footpoint, recorded by GOES between 16:03:34–16:03:44 and shown in Figure 1, were of an event that physically occurred on the Sun at approximately 15:55 UT. Hence, we assume that the initial beam of relativistic particles was accelerated at the Sun shortly after 15:55 UT and observed by the Fort Smith neutron

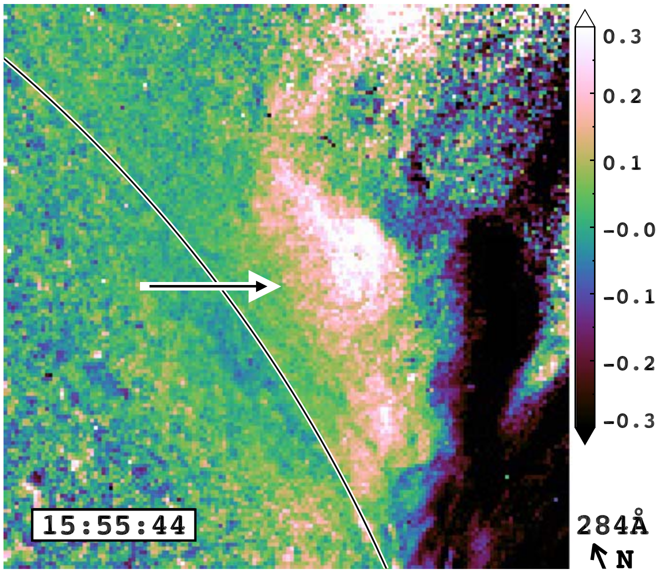

Figure 3. At its base, the large-scale coronal wave visibly refracts, or bends, toward the solar surface; the solar surface is indicated by the white/black lines. In this running relative-difference image, the wave front is the bright, curved, white/pink feature indicated by the arrow. The wave is propagating along the solar surface, toward the upper left-hand corner of the image. Clearly, at this moment, the degree of refraction is significant.

monitor at 16:10 UT, resulting in a particle-travel time of not more than 15 min. This is roughly equal to the time needed for a 450 MeV proton to travel from the Sun to Earth along the Parker spiral.

Viewing the LSCW in cross section at the solar limb allows us to infer some of its qualitative features. A zoomed-in view of the LSCW near the solar surface, taken shortly after the wave onset, at 15:55:44 UT and detected in 284 Å, is shown in Figure 3. Figure 4 shows two additional views of the LSCW, detected in 284 Å and 304 Å, at around 16:04 UT, the time—though not the location—at which the LSCW intersects the footpoint of the Parker spiral. A fundamental feature of the LSCW, which is visible in all these images, is the bending, or refraction, of the wave front base toward the solar surface. The refracting wave front is indicated by an arrow in these images. The opportunity to observe the base of the LSCW, as it refracts toward the solar surface, is one of the remarkable aspects of this event; basically, the location of AR 12673 near the solar limb fortuitously enabled a clear line-of-sight from Earth-bound satellites through the base of the LSCW. If the LSCW had originated farther to the east, the base of the LSCW would have been projected onto the solar disk, making it difficult to disentangle from all the other activity occurring on the solar disk. If the LSCW had originated farther to the west, the base of LSCW would have been hidden behind the solar limb.

Quantitative analysis of the LSCW by Veronig et al. (2018) has shown that the wave speed increases with height above the solar limb. Using SUVI images, they considered separately wave propagation northward and southward of the CME. For the northward-propagating wave, the speed increased from 750 km s^{-1} at 0.05 $R_{\odot}$ to 1200 km s^{-1} at 0.5 $R_{\odot}$. For the southward-propagating wave, the speed increased from 750 km s^{-1} at 0.05 $R_{\odot}$ to 950 km s^{-1} at 0.3 $R_{\odot}$. In other words, the base of the LSCW is dragging along the solar surface, causing it to bend toward the surface of the Sun.

Based on Figure 4, we estimate that the angle between the solar surface and wave front, at the time the LSCW intersects the footpoint of the Parker spiral, is ∼45°. However, as is clearly discernible from Figure 3, the angle between the solar surface and wave front may be much less, perhaps as low as 10–15°, indicating that the degree of refraction can vary widely as the LSCW propagates through various solar features.

The inclined wave front shown in Figures 3 and 4, which is dragging along the solar surface, is part of a larger, dome-shaped wave that eventually encompasses the entire Sun. Three-dimensional, dome-like extensions of coronal waves were first described by Narukage et al. (2004) in X-rays, by Kienreich et al. (2009), Patsourakos & Vourlidas (2009), Veronig et al. (2010) in EUV, and by Kwon et al. (2013) in white light. An example of the full dome is shown in Figure 5. At 16:00 UT, within the LASCO/C2 field of view, the upper dome of the LSCW is barely visible, appearing as a thin halo—the arrow indicates an arbitrary point of the halo, which is colored green—that surrounds the much brighter CME. By 16:12 UT, the entirety of the LSCW is clearly visible as a diffuse feature that surrounds the CME, indicating that it has expanded laterally relative to the CME.

3. Quasi-parallel and -perpendicular Acceleration via a Large-scale Coronal Wave

Diffusive shock acceleration, which is considered to be the most likely, even dominant, contributor to the production of intense particle events (Desai & Giacalone 2016), can take place anywhere along the dome-shaped wave observed during the solar eruption of 2017 September 10 and shown in Figure 5. A schematic picture illustrating the dome-shaped wave is shown in Figure 6. The dome-shaped wave, or LSCW, is depicted by the multicolored, solid line that surrounds the balloon, labeled “CME.” The Sun is the gray, marbled region at the bottom of the picture. The various dashed lines represent magnetic field lines, and the two arrows are two shock normals. Particle acceleration along the top of the dome, in the red zone that extends out from the nose of the LSCW, is usually identified as acceleration by the CME-driven shock. In the context of the solar eruption of 2017 September 10, particle acceleration by the CME-driven shock has been considered by numerous authors, as reviewed in Section 1.

In this paper, our primary focus is on the two-step particle acceleration process that starts at the base of the LSCW and continues at the dome of the LSCW. This acceleration scenario occurs in the green zone of Figure 6 and will be discussed in detail in Sections 4 and 5.

We note that quasi-perpendicular shock acceleration of solar particles at the flank of the LSCW, in the blue zone of Figure 6, has not been considered in the context of this event by any researchers, thus far. Hence, for completeness, we briefly consider this process now. It is worth noting that, within the general theory of diffusive shock acceleration, it is accepted that quasi-perpendicular shock acceleration is a particularly efficient mechanism for producing high-energy particles; therefore, GLEs may benefit from this shock acceleration mechanism (Tylka et al. 2005).

A possible confounding issue for quasi-perpendicular acceleration is the so-called injection problem, which suggests that the minimum particle speed needed to participate in shock acceleration should be higher for quasi-perpendicular shocks than for quasi-parallel shocks. Giacalone (2005a, 2005b, 2017)

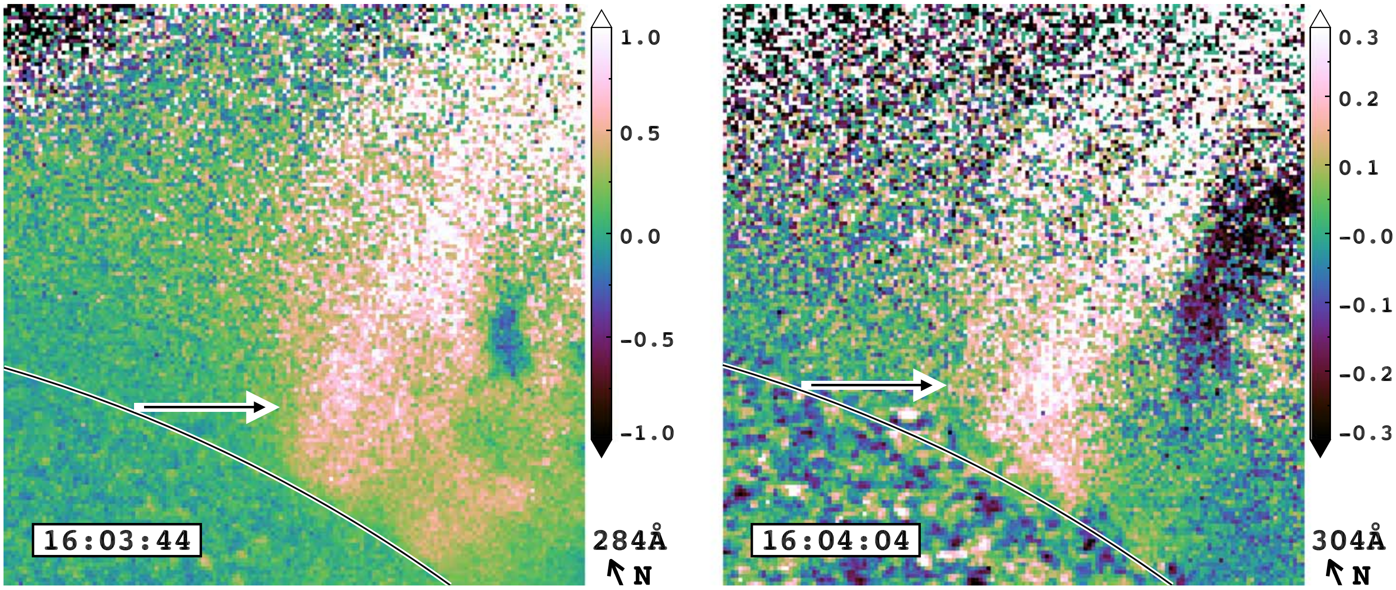

(a) (b)

Figure 4. An additional example of the large-scale coronal wave refracting toward the solar surface at the time when the wave is likely to have intersected the footpoint of the Parker spiral. Similar to Figure 3, the wave front in the running relative difference image is the curved white/pink feature indicated by the arrow, and the solar surface is indicated by the white/black lines. Also similar to Figure 3, the wave is propagating along the solar surface, toward the left-hand edge of the image. Note that the color scale used in the two images, both from GOES-16, the left at 284 Å and the right at 304 Å, are different. Also, note that the color scale used in this 284 Å image is different from the color scale used in 284 Å image shown in Figure 3.

—see also the review by Guo et al. (2021)—has shown that ambient, solar-wind, upstream turbulence significantly enhances trapping near a shock, including quasi-perpendicular shocks, which mitigates the injection problem; however, the modeling used by Giacolone applies specifically to interplanetary shocks. Tylka et al. (2005) and Tylka & Lee (2006) have argued that, near to the Sun, the injection problem for quasi-perpendicular shocks must exist in order to explain certain observed elemental composition ratios seen in many solar eruptions. In addition, their model also requires a compound seed population consisting of coronal and flare suprathermal particles. Then the higher injection speed at quasi-perpendicular shocks determines which suprathermal component will dominate in providing seed particles for high-energy solar eruptions, such as GLEs, thereby explaining observed spectral characteristics in Fe/O and ^{3}He/^{4}He, and mean ionic charges. For example, Tylka et al. (2005) found that 33 of 38 GLEs, or 87%, had measured Fe/O at more than twice the nominal coronal value at energies of $\geqslant$40 MeV /n.

During the solar eruption 2017 September 10, Cohen & Mewaldt (2018) and Mishev et al. (2018) report a low Fe/O ratio at both 12–45 MeV/n and 50–100 MeV/n. This indicates that the Tylka et al. (2005) and Tylka & Lee (2006) mechanism is unlikely to be operative during this solar eruption, perhaps because the seed population was insufficient in terms of size and/or energy. Consider that, although there were 46 solar flares between September 4 and 9, all but three of them were C- or M-class flares; such minor flares may be insufficient to create a seed-particle population. Furthermore, the three X-class flares occurred on September 6 and 7, which may be too far in advance of the September 10 solar eruption, resulting in diffusion of the seed-particle population. Finally, all the flares that were observed from September 4 to 9 originated in NOAA AR 12673, which was also the source of the September 10 event; therefore, any seed particles that might be present would have rotated along with the active region, placing the seed particles downstream from the shock, with the LSCW receding from the seed particles. Taken altogether, these reasons may explain the lack of a flare-associated seed-particle population that could be accelerated by the quasi-perpendicular shock at the flank of the LSCW.

Although clear evidence for acceleration of protons at the flank of the LSCW is lacking, Type II radio emissions provide clear evidence for the acceleration of electrons, which are frequently observed to originate near the flanks of their associated CMEs (Krupar et al. 2019). For the event of 2017 September 10, radio shock signatures, including herringbones, were observed by the Low Frequency Array (LOFAR) at the southern flank of the LSCW shortly after 15:59 UT and at the northern flank of the LSCW after 16:04 UT (Morosan et al. 2019). Other estimates for the onset of the metric Type II burst vary from 15:53 UT, shortly after the onset of the LSCW, to 16:08 UT. For example, Gopalswamy et al. (2018) and Guo et al. (2018) state that a shock-related Type II-like emission started around 15:53 UT. Zhao et al. (2018) place the onset time of the Type II radio burst slightly later than 16:03 UT, whereas Augusto et al. (2019) and Kurt et al. (2019) place the start of the emission at 16:08 UT.

4. Two-step Particle Acceleration via a Large-scale Coronal Wave

Having considered quasi-parallel particle acceleration at the LSCW nose and points extending out from there—the red zone—and quasi-perpendicular particle acceleration at the LSCW flank—the blue zone—we finally turn our attention to the main point of this paper, which, as we will see, involves two steps of oblique particle acceleration, first at the base of the LSCW and again at the upper dome—the green zone.

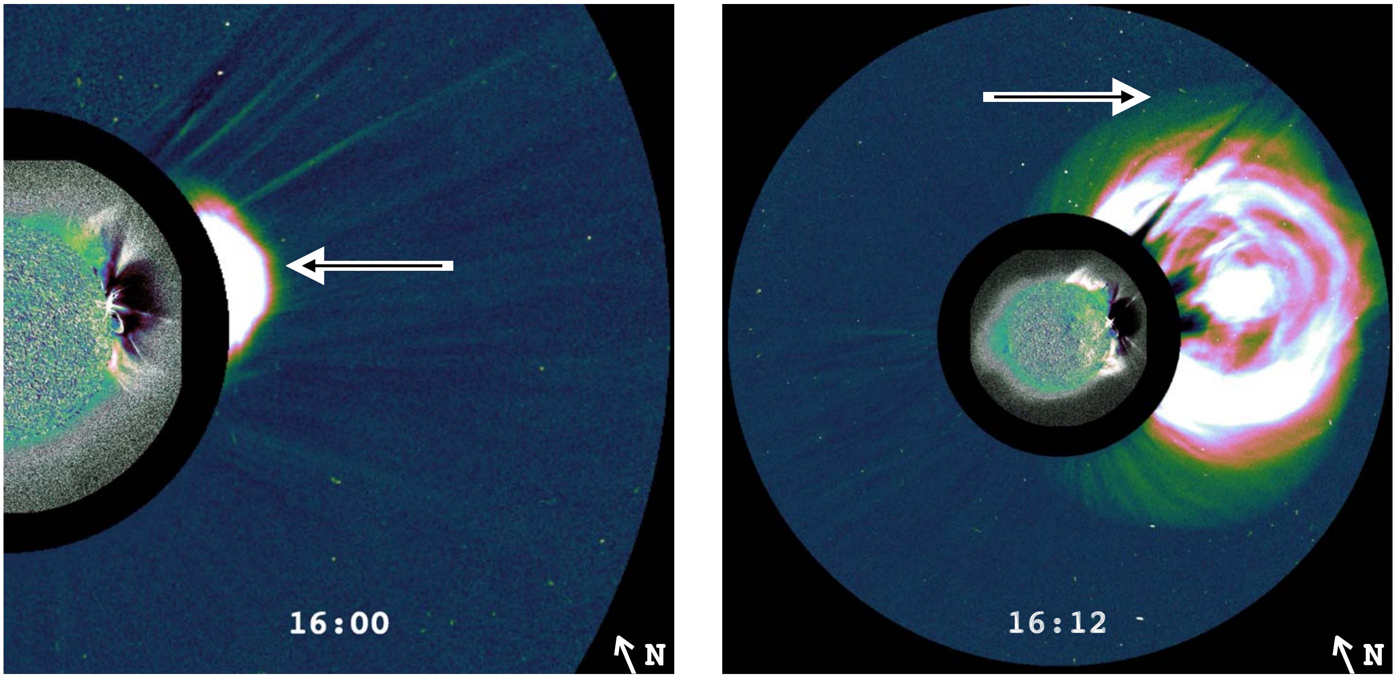

(a) (b)

Figure 5. The large-scale coronal wave, detected in multiple SUVI wavelengths and shown in Figures 1, 3, and 4, is the near-surface manifestation of an encompassing dome-shaped wave. Panels (a) and (b) are, respectively, snapshots of the dome-shaped wave four minutes before and eight minutes after the refracted base of the wave intersects the Parker spiral magnetic field. These composite fixed relative-difference images combine LASCO/C2 and SUVI/195 Å. The black ring separating the SUVI and C2 portions of the composite image is from the C2 occulting disk. The observing times for the different instruments have been matched as closely as possible. In the LASCO/C2 portion of the images, the arrows indicate an arbitrary point of the outer envelope of the dome-shaped wave that appears as a green halo surrounding the bright CME.

Energetic particle acceleration by a refracting wave, such as the base of the LSCW, has been considered by Vainio & Khan (2004). As they themselves state, and as shown in Figure 6, the geometry of their model results in an observer being magnetically connected with the downstream region of the initial shock wave (Vainio & Khan 2004). Although lacking quantitative analysis, Vainio & Khan (2004) also describe a two-step particle acceleration process in which the protons escaping downstream from the refracting LSCW are injected into the outward moving dome of the LSCW. Thus, the refracting shock near the solar surface provides a preacceleration mechanism for the outward-moving shock, helping it to accelerate protons up to GeV energies.

Vainio & Khan (2004) estimate that the spectral-cutoff energy of downstream particles accelerated at a refracting shock is

$$E_c \sim \frac{\rho_{sc}-1}{\rho_{sc}}\, m\beta_A\, \frac{(M+\cos\theta_n)^2}{M\cos\theta_n}\, \frac{z_0}{\lambda_0}, \tag{2}$$

where ρ_{sc} is the scattering-center compression ratio, which is the speed, relative to the shock, of the magnetic irregularities in the ambient plasma relative to the shocked plasma; m is the particle mass in MeV; $\beta_A = V_A/c$ is the Alfvén speed, V_A, normalized by the speed of light, c; θ_n is the angle between the shock normal and the upstream magnetic field; $M = V_S\cos\theta_n/V_A$ is the Alfvénic Mach number of the shock, which depends on the radial shock speed, V_S; z_0 is the height above the solar surface at which the shock first intersects the observers magnetic field line, which is related to the available acceleration time; and λ_0 is the particle scattering mean free path.

Following Vainio & Khan (2004), we set $\rho_{sc} = 2$, which results in a differential particle intensity at the shock of $p^{-(\rho_{sc}+2)/(\rho_{sc}-1)} = p^{-2}$, where p is the particle momentum. The values of V_S and θ_n are derived from the observations: Based on the solar limb view shown in Figure 4, we assume that $\theta_n \sim 45°$. If the LSCW reached the Parker spiral footpoint—assumed to be 40° west of the Sun–Earth line—at 16:04 UT, and if the LSCW was first observed around 15:52 UT (Liu et al. 2018), then the wave speed along the solar surface is ~840 km s^{-1}; this is similar to the speed calculated by Liu et al. (2018) and Veronig et al. (2018), but faster than the speed calculated by Hu et al. (2019), who estimated the wave speed as 700–750 km s^{-1}. Given the observed value of θ_n, the radial shock speed is $V_S \sim 840$ km s^{-1}. Vainio et al. (2014) studied a simple, semi-empirical model of the foreshock region of a propagating interplanetary shock driven by a fast CME; they showed that, if particle acceleration occurs near the shock front, $z_0 \sim 0.1R_\odot$, then $\lambda_0 \sim 0.01R_\odot$. On the other hand, if particle acceleration occurs over a broader range of distances from the shock, $z_0 \sim 1R_\odot$, then the scattering mean free path also increases, $\lambda_0 \sim 0.1R_\odot$. Although z_0 and λ_0 vary considerably, the ratio $z_0/\lambda_0 \sim 10$ remains approximately constant. Although the value of this ratio is strictly correct for interplanetary conditions only, we assume that turbulence conditions that impact acceleration near the solar surface are at least as effective as in interplanetary space. If we assume that the Alfvén speed is at most 500 km s^{-1}—this is the representative value assumed by Vainio & Khan (2004) for the acceleration region—then $M \sim 1$ and $E_c \sim 33$ MeV. The closer the

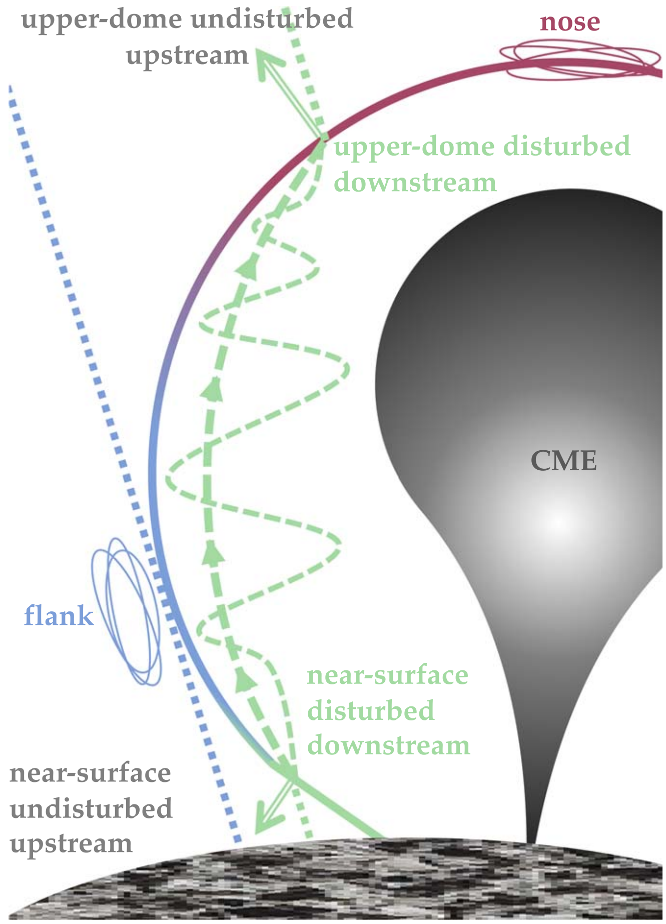

Figure 6. A schematic picture of the large-scale coronal wave (LSCW), which propagates laterally across the solar surface. The gray, marbled region is the Sun; the bubble-like structure extending above the solar surface of the Sun, outlined by the colored, solid line, is the LSCW; the balloon in the right half of the picture is the CME; the various dashed lines represent magnetic field lines; and the two arrows are two shock normals. The significance of the different regions of the schematic, including the various colors, are explained in the text, starting in Section 3 and continuing through Section 5. Note that this schematic is not drawn to scale.

acceleration region is to the solar surface, the lower the Alfvén speed will be; for a fixed shock speed of 840 km s^{-1}, $E_c \rightarrow 12$ MeV as $V_A \rightarrow 0$.

During the solar eruption of 2017 September 10, a second shock, propagating ahead of the CME, was clearly observed by LASCO/C2 as shown in Figure 5; see also the schematic picture in Figure 6. Thus, the 10–30 MeV particles that escape downstream from the refracting shock near the solar surface and stream outwards from the Sun will become a seed population for additional acceleration. Based on the model of Vainio & Khan (2004), the initial particle acceleration by the refracting shock front occurs near the side of the LSCW dome; therefore, it is reasonable to assume that reacceleration at the top of the dome will also occur at the side, well away from the nose of the LSCW dome. Although the shock front well away from the nose of the LSCW dome may be highly oblique, Zank et al. (2006) have shown that even a quasi-perpendicular shock at 0.1 au can boost a particle’s energy by a factor of ~100—see their Figure 7. Thus, protons with energy from 10–30 MeV that are injected into an oblique shock could attain a maximum energy of 1–3 GeV. A similar ∼100-fold increase in particle energy was obtained two decades earlier by Decker & Vlahos (1986)—see their Figure 7, also—wherein they describe particle acceleration during solar flares by oblique shocks.

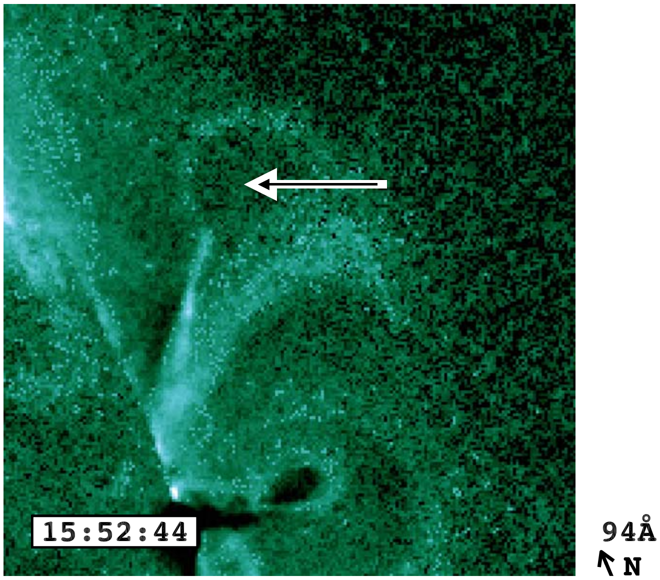

Figure 7. An intrinsic brightness image of the very early stage of the coronal wave observed by SUVI in the 94 Å channel on 2017 September 10. Our analysis suggests that the coronal wave was launched less than a minute prior to this observation. The upstream region, wherein the particles travel on their way from the first-stage acceleration at the refracted base of the coronal wave to the second-stage acceleration at the nose of the wave, is indicated by the arrow.

Under the two-step acceleration mechanism, particle acceleration takes place initially at the location of the refracted shock wave at the base of the LSCW, which is moving laterally across the solar surface and will, in general, be well-separated from the flare site or the nose of the CME-driven shock. Thus, when the LSCW passes over the Sun–Earth footpoint, the protons that are downstream from the refracted shock near the solar surface and that are subsequently reaccelerated at the upper dome will be measured at Earth as GLE protons, despite the poor magnetic connection between the flare site and Earth. This is in contrast to the standard picture, in which protons are accelerated in a one-step process at or near the nose region of a CME shock—the red zone in Figure 6—and then diffuse via pitch-angle scattering or field-line wandering to field lines that are magnetically connected to the observer. Since the refracted shock wave at the base of the LSCW is moving, whereas the Sun–Earth connection point is stationary, the time profile of the injected solar cosmic rays depends on the ability of the seed particles to reach not just the upper dome of the LSCW, but a particular point on the upper dome of the LSCW. If the seed particles are limited to spiraling around the coronal magnetic field lines, which may be twisted or tangled, then the temporal profile of injected particles will likely be short. However, if the seed particles can also undergo some cross-field diffusion while under the dome of the LSCW, then the temporal profile can last longer. Hence, this arrangement for accelerating particles could result in a burst of relativistic protons injected directly onto the Sun–Earth field line. If, in addition, the heliospheric transport was relatively scatter-free, then a neutron monitor at Earth whose asymptotic cone was aligned with the Sun–Earth field line, namely Fort Smith during GLE # 72, could observe a so-called prompt component with a rapid onset and a significant anisotropy. As the LSCW moves on, the number of protons accelerated via the two-stage acceleration mechanism and injected directly onto the Sun–Earth field line will start to decay. However, the shock at the upper dome that is propagating ahead of the CME will continue to accelerate protons at various points along its shock front, resulting in the delayed component of the GLE that will be more isotropic.

5. Implications Derived from Two-step Particle Acceleration

Nature provides many frameworks for diffusive shock acceleration of particles. Based on the temporal sequence of events observed on 2017 September 10, by SUVI and ground-based neutron monitors, we have enlarged on a two-step shock acceleration mechanism created by an LSCW (Vainio & Khan 2004) that can account for protons with GLE energies, which has not been commented on previously. In addition to an LSCW providing an explanation for the prompt arrival of GLE protons at Earth despite the poor magnetic connection between the flare site and Earth, the inclusion of LSCWs as an accelerator of relativistic solar particles allows for several other conclusions and suggestions.

As the LSCW sweeps across the solar surface, it eventually intersects the magnetic field line of every imaginable observer; therefore, an LSCW provides a natural explanation for the wide range in longitude that is observed in many SEPs. However, it is important to keep in mind that, as the LSCW sweeps across the solar surface, the details of the two-step acceleration process will depend on both the local characteristics of the LSCW and local solar conditions at the footpoint of any particular observer. Liu et al. (2018) and Hu et al. (2019) describe variations in the speed and intensity of the 2017 September 10 LSCW on the solar disk and limb. They point out that, when the wave was initially seen on the disk, its wave front was circular. However, their analysis showed that this simple front was interrupted by a cluster of strong magnetic-field regions slightly northeast of the eruption site at AR12673. In addition, they describe reflected and refracted secondary waves from the two polar coronal holes. Interactions of these secondary waves with the primary LSCW, including the possibility of counter-propagating waves, can result in plasma heating by turbulence generation and dissipation (Liu et al. 2018).

Such variations in the local solar conditions and local properties of an LSCW will naturally result in local variations in the two-step acceleration process. In the same way, just as there are local variations in a single LSCW, there are likely significant variations between different LSCW events. Hence, not every LSCW or part of an LSCW will accelerate particles to GLE energies; for example, relativistic solar protons will only be measured at Earth if conditions at the Sun–Earth magnetic footpoint are advantageous. Even in LSCW events that do accelerate particles to GLE energies, such as the 2017 September 10 event, not every region of field lines affected by the LSCW will be suitable for relativistic particle acceleration. For example, at a later stage in the event, when the LSCW may have been weaker, it did not accelerate any high-energy particles in the region magnetically connected to STEREO-A. To summarize this point, spatiotemporal variations in solar and LSCW characteristics, or variations in solar and LSCWs characteristics across different events, may explain variations in the temporal profile and energy spectrum of SEPs and GLEs.

Thus far, we have assumed that particles are initially accelerated at the base of the LSCW, and that these seed particles are then transported downstream and outward to the upper dome of the LSCW, where they are reaccelerated to GeV energies and deposited on open field lines connected to an observer. Since the initial acceleration occurred at the base of the LSCW, these particles must originate from a low-corona particle population. But this picture can be inverted. That is, the first acceleration step could take place at the upper dome of the LSCW. For a large enough LSCW, these particles would then be drawn from a high-corona particle population. Particles downstream of the upper dome of the LSCW—that is, inside the dome—would then stream to the base of the LSCW. If these particles bounce back to the upper dome, they can be reaccelerated to GeV energies and be deposited on open field lines connected to an observer. Thus, two-step, or more strictly, multi-step acceleration by an LSCW can result in a particle composition for any one event that is neither strictly near-surface nor coronal in origin.

Finally, as shown by the cartoon in Figure 6, we reiterate that three distinct modes of acceleration can originate from a single LSCW: (1) quasi-parallel acceleration near the nose of the wave; (2) quasi-perpendicular acceleration near the flank of the wave; (3) two-step oblique acceleration that starts at the refracted base of the coronal wave, producing downstream seed particles that are subsequently reaccelerated at the upper dome of the wave up to GeV energies—this takes place within a limited region only, i.e., under the LSCW dome but outside the magnetically distinct CME.

A possible fourth mode of acceleration occurs for a very limited time only, shortly after the coronal wave has been newly launched. This mode is a special case of mode (3), mentioned above. Actual observation of a wave at this very early stage is shown in Figure 7 during the event of 2017 September 10. Very early on in the wave evolution, the refracted base of the wave, which is typically near the flank of the wave, is also aligned with the nose of the wave. That means that particles accelerated at the refracted base can undergo second-stage acceleration at the nose; that is, the downstream seed particles can undergo *parallel* second-stage acceleration. As the wave matures, the second-stage acceleration at the upper dome of the wave will become progressively more oblique, and will be described by mode (3) above. Thus, in a "baby" coronal wave, the two-step acceleration will be much more efficient than in the later stages. Now, the baby stage lasts only for a very short time, so the seed particle energy will be comparatively lower. But the improved efficiency of parallel-shock acceleration relative to oblique-shock acceleration will more than make up for the reduced seed particle energy. Based on the calculations of Zank et al. (2006)—their Figure 7—we suggest that, during the "baby" coronal wave stage, particles may be accelerated up to 100 GeV. Since this acceleration mode is a special case of mode (3), it also takes place within a limited region only. This region, which is under the LSCW dome but outside the magnetically distinct CME, appears as the inside of a teacup handle in Figure 7 and is indicated by an arrow.

Observations of very high-energy particles have been previously reported. However, many of these observations are of marginal statistical value—signals that are 3σ–4σ above background (Schindler & Kearney 1972, 1973; Karpov et al. 1998). There are three very high-energy bursts that are statistically more significant—signals that are $\geqslant 5\sigma$ above background; these bursts were observed by the Baksan

Underground Scintillation Telescope on 12 October 1981, 29 September 1989, and 15 June 1991 (Karpov et al. 1998). Unfortunately, for these older events, observations are limited; hence, association with an LSCW as cause of particle acceleration is impossible.

6. Conclusion

During GLE # 72, which was part of the solar eruption of 2017 September 10, solar cosmic rays were first observed by the neutron monitor at Fort Smith, because its asymptotic cone was most nearly aligned with the interplanetary magnetic field. The Fort Smith neutron monitor observed a rapid onset of the GLE; however, all the other stations with a low cutoff rigidity in the neutron monitor network observed the start of this GLE delayed by 10 minutes or more relative to Fort Smith, and/or these stations observed a gradual increase, rather than a rapid onset, in the GLE count rate. This was true even for neutron monitors with nearby asymptotic cones.

This anisotropy in the GLE count rate suggests relatively scatter-free propagation, which in turn suggests particle acceleration and injection near the base of the Sun–Earth field line. We have used the excellent SUVI observations of a solar eruption on 2017 September 10 to sketch a scenario in which a shocked coronal wave can accelerate particles up to hundreds of MeVs or even GeV energies. The particle acceleration occurs in two stages, starting at the refracted base of the coronal wave to produce a seed particle population that is subsequently reaccelerated up to relativistic energies. A beam of particles would be observed by the Fort Smith neutron monitor when the LSCW intersected the Sun–Earth footpoint. The weakening anisotropy observed by the Fort Smith neutron monitor is consistent with a prompt injection that has a burst-like intensity–time profile that decays with time as the LSCW continues traveling to the east of Sun–Earth footpoint.

The acceleration mechanism just summarized is meant to describe only the first-to-arrive anisotropic pulse observed by the Fort Smith neutron monitor. Separating the GLE intensity–time profile into an anisotropic, burst-like phase and an isotropic, more gradual phase puts this GLE into the bigger picture of high-energy impulsive GLEs first described by McCracken et al. (2012). The details of the gradual acceleration phase are beyond the scope of this paper. As recounted in Section 1, there are multiple combinations of transport and acceleration processes that can be postulated to qualitatively match the totality of the neutron monitor observations. However, because the relevant indirect evidence is far from being conclusive, it is not straightforward to determine which of these scenarios most closely matches the reality on the Sun. Therefore, as we continue to analyze and model past and future GLEs and large SEPs, it is important to consider all possible acceleration mechanisms that may be operative at the Sun, including the potential role of LSCWs—not forgetting the near-surface, refracted portion of the LSCW—as well as those of flares and CME-driven shockwaves.

CADK's research at NOAA/SWPC was supported by AFOSR grant FA9550-14-1-0401, and by NASA LWS Grant NNX15AF39G. D.B.S. acknowledges support for CIRES's GOES-R activities via NOAA cooperative agreement NA17OAR4320101. We acknowledge the GLE database (gle.oulu.fi) maintained by the University of Oulu, Finland, and the NMDB database (www.nmdb.eu) founded under the European Union's FP7 program (Contract no. 213007), for providing data. Specifically, the neutron monitor data from Fort Smith are provided by the Bartol Research Institute and the University of Delaware Department of Physics and Astronomy.

Facilities: GOES, SUVI; SOHO, LASCO; NMDB.

Software: IDL, SolarSoft.

ORCID iDs

Curt A. de Koning https://orcid.org/0000-0002-9577-1400
Daniel B. Seaton https://orcid.org/0000-0002-0494-2025

References

Augusto, C. R. A., Navia, C. E., De Oliveira, M. N., et al. 2019, PASP, 131, 024401

Berger, T., Matthiä, D., Burmeister, S., et al. 2018, SpWea, 16, 1173

Bieber, J. W., & Evenson, P. 1995, in 24th Int. Cosmic Ray Conf., ed. N. Iucci & E. Lamanna (Singapore: IUPAP), 1316

Bruno, A., Christian, E. R., de Nolfo, G. A., Richardson, I. G., & Ryan, J. M. 2019, SpWea, 17, 419

Chamberlin, P. C., Woods, T. N., Didkovsky, L., et al. 2018, SpWea, 16, 1470

Chertok, I. M. 2018, Ge&Ae, 58, 457

Cliver, E. W. 2001, in AIP Conf. Proc., 516, 26th Int. Cosmic Ray Conf. (Melville, NY: AIP), 103

Cliver, E. W., Kahler, S. W., Neidig, D. F., et al. 1995, in 24th Int. Cosmic Ray Conf., Vol. 4 (Singapore: IUPAP), 257

Cohen, C. M. S., & Mewaldt, R. A. 2018, SpWea, 16, 1616

Decker, R. B., & Vlahos, L. 1986, ApJ, 306, 710

Desai, M., & Giacalone, J. 2016, LRSP, 13, 3

Gary, D. E., Chen, B., Dennis, B. R., et al. 2018, ApJ, 863, 83

Giacalone, J. 2005a, ApJ, 624, 765

Giacalone, J. 2005b, ApJL, 628, L37

Giacalone, J. 2017, ApJ, 848, 123

Gopalswamy, N., Yashiro, S., Makela, P., et al. 2018, ApJL, 863, L39

Goryaev, F. F., Slemzin, V. A., Rodkin, D. G., et al. 2018, ApJL, 856, L38

Guo, F., Giacalone, J., & Zhao, L. 2021, FrASS, 8, 27

Guo, J., Dumbović, M., Wimmer-Schweingruber, R. F., et al. 2018, SpWea, 16, 1156

Hu, H., Liu, Y. D., Zhu, B., et al. 2019, ApJ, 878, 106

Jiggens, P., Clavie, C., Evans, H., et al. 2018, SpWea, 17, 99

Karpov, S. N., Miroshnichenko, L. I., & Vashenyuk, E. V. 1998, Il NCim, 21, 551

Kienreich, I. W., Temmer, M., & Veronig, A. M. 2009, ApJ, 703, L118

Kocharov, L. G., Lee, J. W., Zirin, H., et al. 1994, SoPh, 155, 149

Kocharov, L. G., Pesce-Rollins, M., Laitinen, T., et al. 2020, ApJ, 890, 13

Kouloumvakos, A., Rouillard, A. P., Share, G. H., et al. 2020, ApJ, 893, 76

Krupar, V., Magdalenić, J., Eastwood, J. P., et al. 2019, ApJ, 882, 92

Kurt, V., Belov, A., Kudela, K., et al. 2019, SoPh, 294, 22

Kurt, V., Belov, A., Kudela, K., & Yushkov, B. 2018, CAOSP Abstracts, 48, 329

Kwon, R.-Y., Ofman, L., Olmedo, O., et al. 2013, ApJ, 766, 55

Lee, C. O., Jakosky, B. M., Luhmann, J. G., et al. 2018, GeoRL, 45, 8871

Li, X., Zhang, J., Yang, S., & Hou, Y. 2019, PASJ, 71, 14

Li, Y., Xue, J. C., Ding, M. D., et al. 2018, ApJ, 853, L15

Liu, W., Jin, M., Downs, C., et al. 2018, ApJL, 864, L24

Long, D. M., Harra, L. K., Matthews, S. A., et al. 2018, ApJ, 855, 74

Longcope, D., Unverferth, J., Klein, C., McCarthy, M., & Priest, E. 2018, ApJ, 868, 148

Mavromichalaki, G., Gerontidou, M., Paschalis, P., et al. 2018, SpWea, 16, 1797

McCracken, K. G., Moraal, H., & Shea, M. A. 2012, ApJ, 761, 101

Miroshnichenko, L. I. 2018, PhyU, 61, 323

Mishev, A. L., & Usoskin, I. G. 2018, SpWea, 16, 1921

Mishev, A. L., Usoskin, I. G., Raukunen, O., et al. 2018, SoPh, 293, 136

Miteva, R., Klein, K.-L., Kienreich, I., et al. 2014, SoPh, 289, 2601

Morosan, D. E., Carley, E. P., Hayes, L. A., et al. 2019, NatAs, 3, 452

Narukage, N., Morimoto, T., Kadota, M., et al. 2004, PASJ, 56, L5

Omodei, N., Pesce-Rollins, M., Longo, F., Allafort, A., & Krucker, S. 2018, ApJL, 865, L7

Park, J., Innes, D. E., Bucik, R., & Moon, Y.-J. 2013, ApJ, 779, 184

Park, J., Innes, D. E., Bucik, R., Moon, Y.-J., & Kahler, S. W. 2015, ApJ, 803, 3

Patsourakos, S., & Vourlidas, A. 2009, ApJ, 700, L182

Perez-Peraza, J. A., Márquez-Adame, J. C., Caballero-Lopez, R. A., & Manzano Islas, R. R. 2020, AdSpR, 65, 663
Polito, V., Dudík, J., Kašparová, J., et al. 2018, ApJ, 864, 63
Rouillard, A. P., Sheeley, N. R., Tylka, A., et al. 2012, ApJ, 752, 44
Schindler, S. M., & Kearney, P. D. 1972, Natur, 237, 503
Schindler, S. M., & Kearney, P. D. 1973, NPhS, 242, 56
Seaton, D. B., & Darnel, J. M. 2018, ApJL, 852, L9
Simpson, J. A., Fonger, W., & Treiman, S. B. 1953, PhRv, 90, 934
Starodubtsev, S. A., Baishev, D. G., Grigoryev, V. G., et al. 2019, STP, 5, 14
Stone, E. C., Frandsen, A. M., Mewaldt, R., et al. 1998, SSRv, 86, 1
Torsti, J., Kocharov, L. G., Teittinen, M., & Thompson, B. J. 1999, ApJ, 510, 460
Torsti, J., Anttile, A., Kocharov, L., et al. 1998, GeoRL, 25, 2525
Tylka, A. J., Cohen, C. M. S., Dietrich, W. F., et al. 2005, ApJ, 625, 474
Tylka, A. J., & Lee, M. A. 2006, ApJ, 646, 1319
Vainio, R., & Khan, J. I. 2004, ApJ, 600, 451
Vainio, R., Ponni, A., Battarbee, M., et al. 2014, JSWSC, 4, A08
Veronig, A. M., Muhr, N., Kienreich, I. W., Temmer, M., & Vršnak, B. 2010, ApJ, 716, L57
Veronig, A. M., Podladchikova, T., Dissauer, K., et al. 2018, ApJ, 868, 107
Warmuth, A. 2015, LRSP, 12, 3
Warren, H. P., Brooks, D. H., Ugarte-Urra, I., & Reep, J. W. 2018, ApJ, 854, 122
Wu, C.-C., Liou, K., Lepping, R., & Hutting, L. 2019, SoPh, 294, 110
Yan, X. L., Yang, L. H., Xue, Z. K., et al. 2018, The ApJL, 853, L18
Zank, G. P., Li, G., Florinski, V., et al. 2006, JGR, 111, A06108
Zhao, M.-X., Le, G.-M., & Chi, Y.-T. 2018, RAA, 18, 74